# Application of Dual-target Computed Tomography for Material Decomposition of Low-Z Materials

Pavel Mikuláček[1,2] · Marek Zemek[2] · Pavel Štarha[1] · Tomáš Zikmund[2] · Jozef Kaiser[2]

## Abstract

The extension of conventional computed tomography known as spectral computed tomography involves utilizing the variations in X-ray attenuation, driven by spectral and material dependencies. This technique enables the virtual decomposition of scanned objects, revealing their elemental constituents. The resultant images provide quantitative information, such as material concentration within the scanned volume. Enhancements in results are achievable through methods that capitalize on the strong correlation among decomposed images, effectively minimizing noise and artifacts. The Rigaku nano3DX submicron tomograph uses a dual-target source, which allows the generation of two distinct X-ray spectra through different target materials. This configuration holds promise for high-resolution applications in spectral tomography, particularly for low-Z materials, where it offers high contrast in the acquired images. The potential of this setup in the context of spectral computed tomography is explored in this contribution, delving into its applications for materials characterized by low atomic numbers.

**Keywords** Computed tomography · Spectral CT · Dual-target · Material decomposition · Low-Z materials · Correlated noise

## 1 Introduction

Spectral computed tomography represents an advancement over traditional computed tomography (CT) by not only providing visualizations of internal structures in scanned objects, but also by enabling the identification, differentiation, and quantification of materials along with their concentrations within these objects [1]. This process, which is known as basis material decomposition (BMD), relies on the X-ray attenuation properties of materials, which vary with both X-ray energy and the specific material [1]. To implement BMD or other spectral CT techniques, two or more datasets with distinct X-ray spectra must be acquired [1]. Dual-energy computed tomography (DECT), a common form of spectral CT, involves using two X-ray spectra with sufficient separation, i.e., minimal spectral overlap [2]. When DECT is performed using a single X-ray source, spectral separation is typically achieved by adjusting the tube voltage and/or filtering [1]. While DECT is well-established in medicine [3], it also finds applications in industrial and laboratory CT, where ongoing developments aim to enhance spectral separation [4, 5].

In this work, existing DECT material decomposition methods are applied to data obtained using a dual-target X-ray source. This variation of DECT is termed dual-target CT (DTCT) throughout this work. In DTCT, measurements are performed not only with different settings of accelerating voltage, but also with different target materials to generate distinct X-ray spectra, and spectral separation is achieved by a change of not only bremsstrahlung, but also characteristic radiation. Therefore, the goal of this work is to explore the feasibility of DTCT measurements for material decomposition and spectral CT processing, with a particular focus on high-resolution scans of low-density, low-Z materials, such as organic compounds. It is presumed that such applica-

✉ Marek Zemek
  marek.zemek@ceitec.vutbr.cz

  Pavel Mikuláček
  Pavel.Mikulacek@vutbr.cz

  Pavel Štarha
  starha@fme.vutbr.cz

  Tomáš Zikmund
  tomas.zikmund@ceitec.vutbr.cz

  Jozef Kaiser
  jozef.kaiser@ceitec.vutbr.cz

[1] Institute of Mathematics, Faculty of Mechanical Engineering, Brno University of Technology, Brno, Czech Republic

[2] Central European Institute of Technology, Brno University of Technology, Brno, Czech Republic

**Fig. 1** Geometry of the Rigaku nano3DX, exaggerated for illustrative purposes
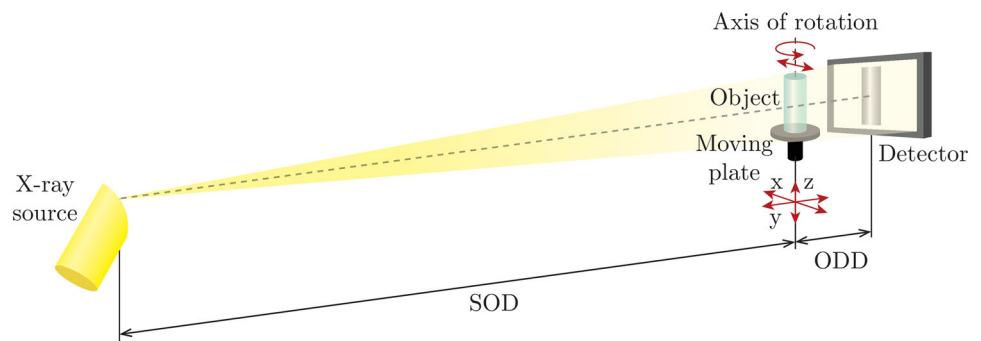


tions of DTCT are feasible, but, to the authors' knowledge, experimental evaluation is currently missing in the existing literature. The particular algorithm used in this work is an existing approach based on entropy minimization to reduce noise in the decomposed data.

## 2 Materials and Methods

### 2.1 Rigaku nano3DX

The Rigaku nano3DX (Rigaku Corporation; Japan) is utilized in this work for the acquisition of DTCT data. It is an X-ray microscope with the capability to conduct CT measurements at submicron resolution, and the MicroMax-007 HF X-ray source with two user-switchable target materials. In this case, the source is equipped with a copper (Cu) and a molybdenum (Mo) target, with a pre-determined accelerating voltage of 40 kV and 50 kV, respectively. The voltages are tuned to optimize the ratio of characteristic radiation and bremsstrahlung, leading to X-ray spectra with prominent peaks at roughly 8.0 keV for Cu and 17.5 keV for Mo (Fig. 2), and effective spectral separation. DTCT measurements on this setup are performed sequentially, with a switch of the target material and accelerating voltage in-between. This switch is automated and it can be completed in several minutes. No other components of the scan geometry move during this time, so although the two measurements are sequential, they are usually well-aligned without the need for substantial image registration during post-processing.

Unlike conventional industrial cone-beam CTs, the nano3DX employs a quasi-parallel X-ray beam, which is achieved through a large source-object distance (SOD) and a relatively small object-detector distance (ODD) (figure 1) [6]. Based on a previous work, the SOD is approximately 263.35 mm [7]. The ODD is adjustable, and is usually set to a few millimeters. Other parameters such as the material and thickness of the scintillation layer are not available. The X-ray image is magnified through optical elements housed in exchangeable units mounted in front of the detector. Subsequently, the magnified image is captured by an XSight
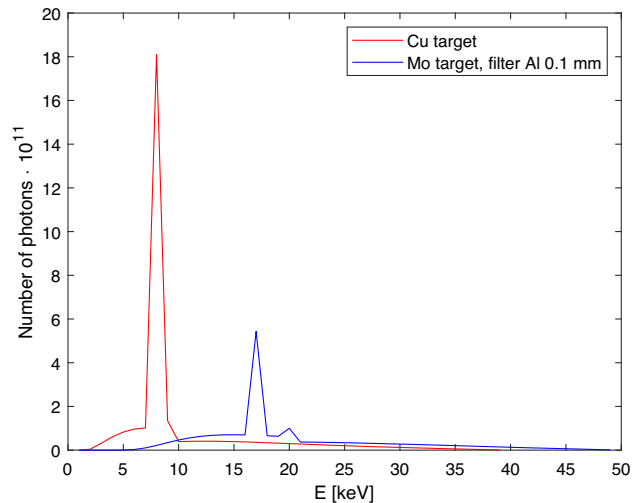


**Fig. 2** X-ray spectrum for the Cu target and Mo target with filter Al 0.1 mm of the nano3DX. The simulation was created in the software aRTist [8]

Micron LC camera (Rigaku Corporation; Japan) equipped with a 3300 x 2500 pixel CCD chip. The chosen optical unit determines the effective pixel size, which ranges from 0.27 $\mu$m to 4.32 $\mu$m (excluding pixel binning) [6].

### 2.2 Material Decomposition

The use of spectral CT can be divided into several categories [1]. For this work, however, the division into two groups is sufficient. The first group are problems in which it is necessary to recognize and distinguish different materials occurring in the investigated object. This can be achieved by using two or more X-ray spectra with different system weight functions (SWFs) [1]. This approach can be described as a classification problem in which the data are segmented based on whether a given material is present at a position or not [5]. In medicine, this segmentation can be used to efficiently distinguish tissues and contrast agents that may otherwise be difficult to separate in conventional CT [3]. The second group consists of questions related to quantitative information about the given material, such as the concentrations of

various compounds and mixtures [9], or the determination of the atomic number and density of the individual components of the material [10].

Alvarez and Macovski [11] described the first basis material decomposition (BMD) algorithm in 1976. Since then, BMD has been the standard decomposition algorithm in spectral CT. Outputs from BMD are nowadays used as initial values for various iterative methods [12]. The main idea of BMD is that the spectral attenuation coefficient $\mu(E, x)$ can be written using a superposition of basis functions

$$\mu(E, x) = c_1(x) f_1(E) + c_2(x) f_2(E) + \ldots + c_n(x) f_n(E), \tag{1}$$

where $c_i$ are concentrations of $N$ different and linearly independent basis material attenuation functions $f_1, f_2, \ldots, f_n$ [1]. It is also assumed that $\sum_{i=1}^{N} c_i = 1$, based on the mixture rule [13].

For DECT, the following system of equations describing the attenuation of X-rays can be obtained:

$$\begin{pmatrix} A_{\text{Cu}} \\ A_{\text{Mo}} \end{pmatrix} = \begin{pmatrix} \int_0^{40} w_{\text{Cu}}(E) \exp\left(-\int_L \mu(E, x)\mathrm{d}x\right) \mathrm{d}E \\ \int_0^{50} w_{\text{Mo}}(E) \exp\left(-\int_L \mu(E, x)\mathrm{d}x\right) \mathrm{d}E \end{pmatrix}, \tag{2}$$

where indices denote measurements for different X-ray spectra, $A$ is the ratio between the output intensity $I$ of the X-ray radiation from the material of thickness $L$ and its initial intensity $I_0$ and $\mu(E, x)$ is linear attenuation coefficient [1]. There are also SWFs in equation (2), which are given by

$$w(E) = \frac{S(E)D(E)}{\int_E S(E)D(E)\mathrm{d}E}, \tag{3}$$

where $S(E)$ is X-ray spectrum for specific measurements [1] and $D(E)$ is detector responsivity [14], which remains unchanged between measurements. Due to the unknown scintillator thickness of nano3DX, it is assumed that D(E) equals 1.0 for all E. Using the superposition described by Eq. (1) the equations (2) can be parameterized and the solutions of the system of integral nonlinear equations thus obtained are the concentrations $c_i$ of the individual materials. Finding a solution to the system (2) is not straightforward, so BMD is performed on the reconstructed data, leading to a system of equations

$$\begin{pmatrix} \overline{\mu}_{\text{Cu}}(x) \\ \overline{\mu}_{\text{Mo}}(x) \end{pmatrix} = K \begin{pmatrix} c_1(x) \\ c_2(x) \\ \vdots \\ c_n(x) \end{pmatrix}, \tag{4}$$

where $\overline{\mu}_i$ are reconstructed data and $K$ is material composition matrix given by the elements [1]

$$K_{i,j} = \int_E w_i(E) f_j(E) dE, \quad i = \text{Cu, Mo}; \quad j = 1, \ldots, n.$$

The system (4) can be easily solved by pseudoinversion [15] to obtain a system of equations

$$\begin{pmatrix} c_1(x) \\ c_2(x) \\ \vdots \\ c_n(x) \end{pmatrix} = K^+ \begin{pmatrix} \overline{\mu}_{\text{Cu}}(x) \\ \overline{\mu}_{\text{Mo}}(x) \end{pmatrix}. \tag{5}$$

This process is referred to as Direct Inversion (DI) [16]. Clearly, in the case of DECT, we have two different datasets occurring on the right-hand side with which we want to find $N$ unknown concentrations, which is an indeterminate system. Therefore, it is best to choose the number of search materials $N = 2$. For increasing number of materials, there is an accumulation of errors, i.e. inaccurate determination of the concentration of a given material.

## 3 Noise Analysis

Jiang [17] states, that the utilization of the direct inversion algorithm significantly diminishes the signal-to-noise ratio (SNR) in decomposed images, adversely impacting the quality of any subsequent analysis. Numerous conventional image denoising algorithms suffer from a common issue of losing information around edges, resulting in blurring. However, specific properties of noise in decomposed images are harnessed by specialized algorithms to effectively mitigate noise without losing image details [17].

### 3.1 Distribution of Noise

The noise analysis is performed on two decomposed materials in the image domain. Two CT datasets acquired with different targets are scanned independently, and their noise is therefore independent [18]. Two values can be assigned to each pixel position. The first, $\mu_{\text{Cu}}$, corresponds to the measurement with the copper target and the second, $\mu_{\text{Mo}}$, to the measurement with the molybdeum target. Given the system of equations (4), one pixel $p$ with respect to position can be expressed as

$$\overline{\mu}_p = K c_p, \tag{6}$$

where $\overline{\mu}_p = (\overline{\mu}_{\text{Cu}}^p, \overline{\mu}_{\text{Mo}}^p)^T$, $c_p = (c_1^p, c_2^p, \ldots, c_n^p)^T$ and $K$ is the material composition matrix [17]. Aside from the

amplification of noise during the material decomposition process, the noise in the resulting decomposed images exhibits a strong correlation [18]. We make the assumption that the noise in individual pixels of both CT datasets follows a normal distribution:

$$\overline{\mu}_p \sim \mathrm{N}(\boldsymbol{K c}_p, \boldsymbol{V}), \tag{7}$$

where $V = \mathrm{diag}(\mathrm{var}(\overline{\mu}_{\mathrm{Cu}}), \mathrm{var}(\overline{\mu}_{\mathrm{Mo}}))$ is a diagonal matrix whose diagonal elements are the noise variance in the first and second CT dataset [19]. Using the DI applied to equation (6) and probability distribution (7) it can be seen that the probability distribution of the concentration of decomposed images is

$$\boldsymbol{c}_p \sim \mathrm{N}\left((\boldsymbol{K}^+\overline{\mu}_p), \boldsymbol{K}^+\boldsymbol{V}(\boldsymbol{K}^+)^T\right), \tag{8}$$

where $\boldsymbol{K}^+$ denotes pseudoinversion (inversion) of material composition matrix [18]. This indicates that the decomposed images share a jointly Gaussian distribution, characterized by an elliptical and highly asymmetric nature, as described by the covariance matrix $\boldsymbol{K}^+\boldsymbol{V}(\boldsymbol{K}^+)^T$. Using SVD decomposition [20], it can be shown that the covariance matrix of the distribution (8) has only two non-zero singular values [18]. This implies that the noise in the multi-material decomposed images is distributed solely in two directions and is absent in the remaining directions.

### 3.2 Reduction of Noise

Petrongolo [18] states, that the entropy of the object under observation serves as a valuable tool for noise reduction in DECT. Entropy is a quantification of "uncertainty" or disorder. In terms of probability, entropy is elucidated as follows: probability distributions with clear distinctions have low entropy, while those with more ambiguity, such as normal distributions, exhibit higher entropy. The Image-domain Decomposition through Entropy Minimization (IDEM) algorithm leverages the correlation among decomposed images to effectively suppress noise [18].

The IDEM algorithm [18] operates on the premise that pixels in decomposed images representing similar materials form clusters in a 2D scatter plot. When noise is minimal, the scatter plot should exhibit tight clusters with distinct centers of mass (COM). In its initial step, the IDEM algorithm identifies the direction (optimized axis) in the 2D scatter plot where the entropy is minimal. This direction is defined by the axis passing through the origin. Subsequently, noise is suppressed in the direction perpendicular to the optimized axis. For each $\boldsymbol{x}$ pixel pair at the corresponding location in the decomposed images, a projection onto the optimized axis

is performed. Pixels indicating similar materials are identified if their projected values fall within a small pre-defined neighborhood around the $\boldsymbol{x}$ projection. The COM, denoted as $\boldsymbol{x}_c$, is calculated for a given group of pixels. The original $\boldsymbol{x}$ value is then replaced with the computed $\boldsymbol{x}_c$ value. In the final step, the pixels are rotated back into the original space. The extent of noise suppression in the COM calculation increases along with the inclusion of more pixels, but this comes at the cost of signal distortion. This phenomenon is akin to the impact observed in other noise reduction techniques, where increased noise suppression leads to a compromise in spatial resolution. Introducing pixel weighting in the COM calculation proves beneficial in mitigating image distortion and enhancing the precision of distinguishing different materials. Pixels with values proximate to those at position $\boldsymbol{x}$ exert a stronger influence, while pixel values significantly distant from the value at location $\boldsymbol{x}$ carry less weight, thus minimizing their impact [18]. For this article, the spatial weighting function used was the same as in the reference [18].

## 4 Testing Data

### 4.1 Simulated Water-Ethanol Phantom

A virtual phantom was created using Autodesk Inventor software (Autodesk; USA) to test material decomposition in a controlled, simulated setting. The phantom comprises six spheres with a diameter of 0.05 mm, evenly distributed on a circle with a diameter of 0.125 mm. The chosen sizes align with the capabilities of the Rigaku nano3DX in terms of resolution. Each sphere contains a different mixture of water ($H_2O$) and ethanol ($C_2H_6O$). Notably, one of the spheres is composed entirely of water, and another is composed of pure ethanol, as illustrated in Fig. 3A. These spheres serve as references. Water and ethanol were deliberately chosen for their similar attenuation properties (Fig. 3B).

Two phantom measurements were simulated for the Cu and Mo targets. Generation of synthetic data was accomplished using the aRTist simulation software (BAM; Germany). The geometry and parameters of the nano3DX were modeled closely (Table 1) to produce realistic images which would help predict the viability of material decomposition in real measurement conditions.

Tomographic reconstruction of the simulated datasets was performed in Matlab (The Mathworks; USA) using the FDK reconstruction algorithm [21] implemented in the ASTRA toolbox [22, 23]. The reconstruction process involved applying a circular masking function to zero out values outside the field of view. The reconstructed CT slices for both targets are shown in Fig. 4.

**Table 1** Input parameters set in aRTist

| Parameter | Value | Parameter | Value |
|---|---|---|---|
| Target material | Cu/Mo | SOD [$\mu$m] | 264 500 |
| Tube voltage [kV] | 40/50 | ODD [$\mu$m] | 500 |
| Tube current [mA] | 30/24 | Environment material | Air |
| Detector height [px] | 500 | Background value | 60 000 |
| Detector width [px] | 500 | Noise factor | 0.01 |
| Pixel size [$\mu$m] | 0.54 | Flat field correction | Yes |

The background value denotes the pixel value corresponding to unattenuated X-rays. A noise factor of 0.01 in the projections was determined through experimental findings, as it approximately corresponds to a normal distribution with a standard deviation of $\sigma \approx 12.7$ for the specified acquisition setting
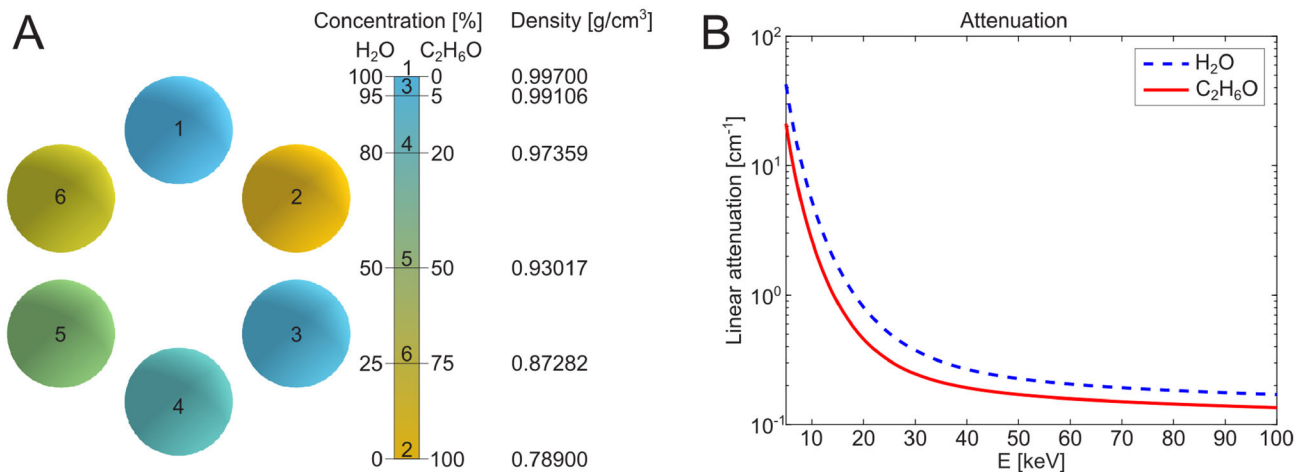


**Fig. 3** 3D model of the synthetic phantom and the composition and density of its spheres (**A**), along with a graph of the linear attenuation of the materials used in creating the phantom (**B**). Concentrations are expressed in volume percentages. Data was created in the software aRTist

**Fig. 4** Reconstructions of simulated data of the synthetic water-ethanol Phantom
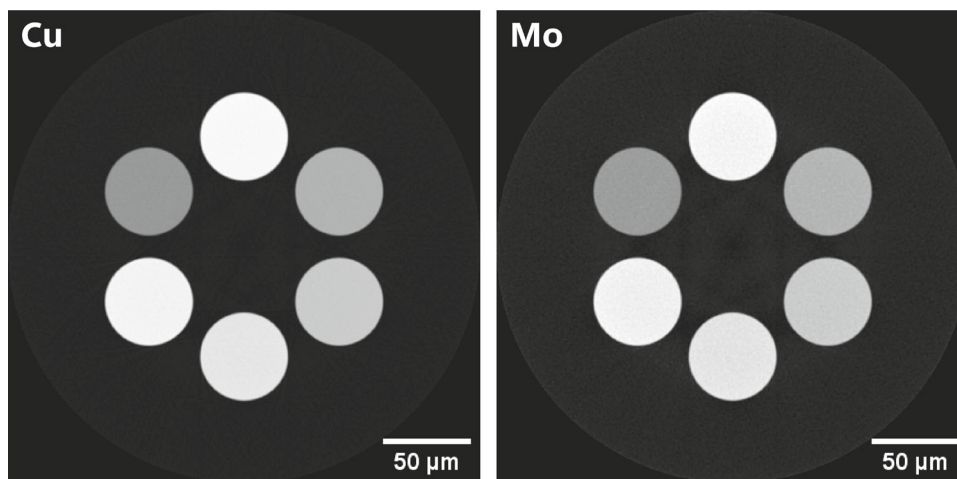


## 4.2 Physical Water-Ethanol Phantom

To test the DTCT on the nano3DX, a real phantom was created based on the one designed for simulated measurements. Seven kapton tubes with diameters of 1 mm were were placed in a bundle, with the central tube serving only as a structural component. The six outer tubes were filled with various mixtures of water and ethanol, corresponding to the same volume percentages as the simulated phantom. The phantom was constructed to resemble the simulated dataset reasonably closely, but its shape and size were modified to take into account restrictions such as the size of the available materials and tools. After the tubes were filled, they were plugged on both sides with dental wax. The ends were wrapped with

**Table 2** Scan settings used for the DTCT measurement of the water-ethanol phantom on the nano3DX

| Measurement | 1 | 2 |
|---|---|---|
| Target | Cu | Mo |
| Tube Voltage [kV] | 40 | 50 |
| Tube Current [mA] | 30 | 24 |
| estimated ODD [mm] | 6.5 | 6.5 |
| Filter | none | 0.1 mm Al |
| Exposure [s] | 0.65 | 0.33 |

parafilm and then glued with hot glue, so as to seal the contents of the tubes from the outside environment. The tubes were then placed on a metal rod, which was then attached to a standard nano3DX sample holder.

Before the actual measurement, the sample was left to stabilize in the measurement chamber of the scanner to minimize unwanted movement during scanning. A high binning setting was applied on the acquired projection images, leading to lower resolution but much shorter scan times, both in terms of exposure and also a lower total number of projections. In this case 300 projections were acquired over a 180° arc for each measurement. The final voxel size of both measurements after binning was approximately 8.34 $\mu$m. The increased measurement speed was useful in the specific case of the water-ethanol phantom, to prevent the liquids from potentially evaporating over the course of a longer measurement. The two DTCT measurements were done sequentially, first for the Cu target, then for the Mo target. Scan settings are summarised in Table 2.

Tomographic reconstruction of the real datasets was performed using version 2.0.3.0 of the proprietary Rigaku reconstruction software. Standard settings of the software were used, including any potential additional processing during the reconstruction process. The axis of rotation of the datasets was corrected manually prior to reconstruction, and no other processing was applied on the data before reconstruction.

In the reconstructed slices in Fig. 5 shows, that kapton has very similar attenuation as water, as in some areas it is not completely distinguishable. Unlike in other DECT approaches, data measured at higher energies (Mo target) contain more noise than data measured using lower energies (Cu target). Additionally, parts of the glue used to fix and seal the phantom can be seen in-between the kapton tubes.

## 5 Results and Discussion

The resulting images of material decomposition applied on the simulated data can be seen in the Fig. 6. The resulting evaluation was performed in six different regions of interest (RoI), one in each sphere of the phantom (Fig. 3). The material decomposition matrix was constructed using the reference regions RoI1 and RoI2, which contain pure water and pure ethanol. The decomposed images without noise filtering can be seen in the Fig. 6a. It is clear that there is a significant increase in noise when DI is applied. The noise degrades the structures of the spheres, especially those with higher ethanol concentration. A beam hardening artifact can also be observed in the data, which is a likely occurrence, due to the homogeneous nature of the phantom. Moreover, beam hardening is generally more likely to occur at lower X-ray energies [24]. Values present in the individual RoIs are listed in Table 3. Although the mean values closely match the known reference concentration values, the high values of standard deviation (STD) make the result very uncertain. This may play a role in further data analysis, making it difficult to clearly identify the boundaries of different regions and possibly skewing the average values, especially when smaller regions are evaluated.

To reduce the influence of noise in the decomposed data, it is necessary to use noise reduction based on the IDEM algorithm, as shown in Fig. 6b. It can be seen that IDEM noise reduction preserves the edges of individual objects well. As a side-effect, there has also been a slight reduction in the beam hardening artifact, which can be seen as a type of specific noise in the data. Table 3 shows the specific values of the concentrations of substances occurring in each sphere, as well as a significant reduction in STDs in all RoIs, with much more acceptable error rates of less than 7%. The reduction in the uncertainty of measured concentrations is visualized in Fig. 7. It is important to note that negative values or values greater than one have no physical meaning in terms of concentrations. As such, values outside the range of 0% and 100% can be treated as invalid, or they can be clipped to fit within this range.

The resulting material decomposition data for the physical phantom are shown in the Fig. 8. As with the simulated data, DI results in a significant increase in noise. This hinders the evaluation of concentrations of water and ethanol in the RoIs. Moreover, beam hardening also causes local distortions of decomposed values. Therefore, reduction of beam hardening artifacts may lead to a potential improvement in the results of material decomposition. Table 4 shows that the standard deviations of the estimated concentration values in the RoIs range from 50% to 90%. Such high deviations cause too much uncertainty in the measurements, and it was therefore necessary to reduce the noise using IDEM. The noise-reduced data are shown in Fig. 8.

The mean concentrations of the RoIs in decomposed images of the physical phantom differ from the concentration values of the simulated data. This is likely because of ethanol evaporating from the phantom during the measurement, despite efforts to seal the tubes during preparation.

**Fig. 5** Reconstructions of real data acquired using the Cu target and the Mo target with Al filter. RoIs are labeled in the reconstruction for the Cu target





(a)                                                          (b)
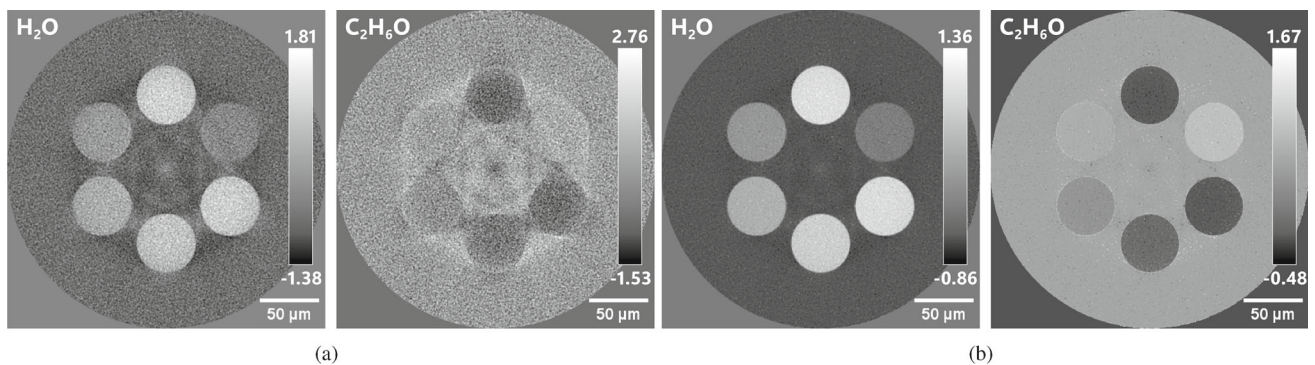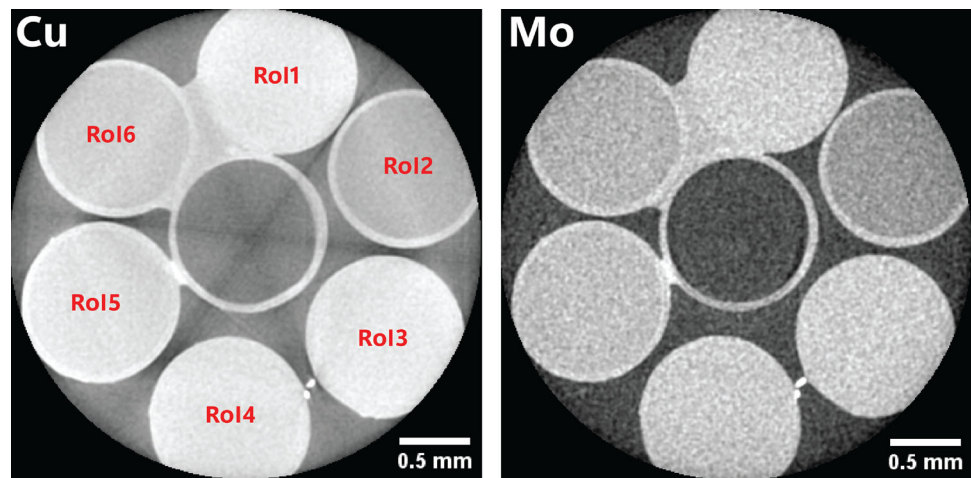
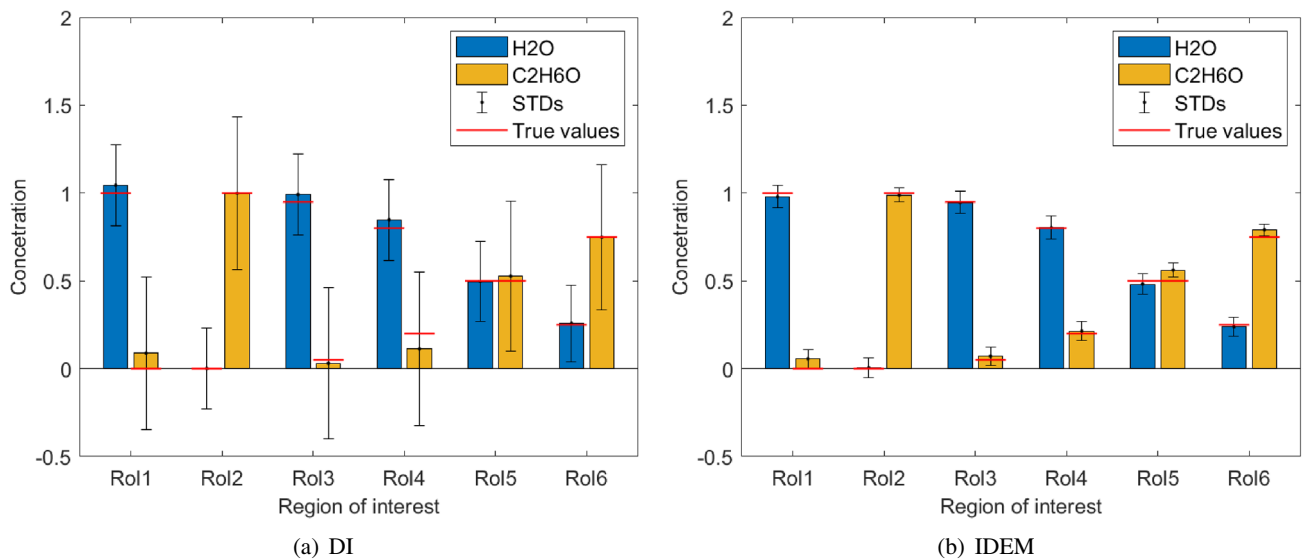**Fig. 6** Synthetic phantom, material decomposition using DI (**a**) and noise reduction using IDEM (**b**)

**Table 3** Mean values of concentrations and STDs in decomposed images for phantom simulations

| RoI | DI $H_2O$ | DI $C_2H_6O$ | IDEM $H_2O$ | IDEM $C_2H_6O$ |
|---|---|---|---|---|
| 1 | $1.045 \pm 0.230$ | $0.088 \pm 0.435$ | $0.979 \pm 0.064$ | $0.056 \pm 0.054$ |
| 2 | $0.001 \pm 0.231$ | $0.999 \pm 0.436$ | $0.005 \pm 0.057$ | $0.988 \pm 0.040$ |
| 3 | $0.992 \pm 0.228$ | $0.031 \pm 0.432$ | $0.946 \pm 0.064$ | $0.071 \pm 0.052$ |
| 4 | $0.848 \pm 0.230$ | $0.113 \pm 0.435$ | $0.803 \pm 0.065$ | $0.214 \pm 0.055$ |
| 5 | $0.496 \pm 0.227$ | $0.527 \pm 0.429$ | $0.482 \pm 0.057$ | $0.561 \pm 0.040$ |
| 6 | $0.258 \pm 0.219$ | $0.749 \pm 0.413$ | $0.238 \pm 0.052$ | $0.791 \pm 0.034$ |

Additionally, evaporation could have also caused the concentrations in individual RoIs to vary between the sequential measurements for the Cu and Mo targets, which could also have affected the results. Despite this, differences in concentrations of the RoIs after the application of IDEM can be distinguished. The achieved results show the feasibility of high-resolution, high-contrast, low-energy material decomposition of low-Z substances using DTCT. The results may potentially be further improved using some of the more advanced material decomposition algorithms based on iterative optimization [12, 19].

Artifacts due to data truncation may also affect the results of material decomposition. These artifacts are common in high-resolution CT, where the scanned objects often do not entirely fit into the field of view (FoV). The erroneous accumulation of material on the edge of the FoV is a typical artifact for FBP-type reconstruction algorithms, and it invalidates the decomposed values on the perimeter of the image. This truncation artifact needs to be corrected or excluded from further analysis, as was the case here. Alternatively, it is possible to correct this artifact by padding the projection data, which may be a more effective approach in terms of preserving the practical extent of the FoV in terms of data validity.

(a) DI

(b) IDEM

**Fig. 7** Results from the Table 3 plotted in a bar graph with STDs and true values

**Fig. 8** Material decomposition using DI and noise reduction using IDEM for data of the prepared phantom. To improve the clarity of values within the relevant interval of 0%–100%, data above and below a certain value were covered by a single-color overlay
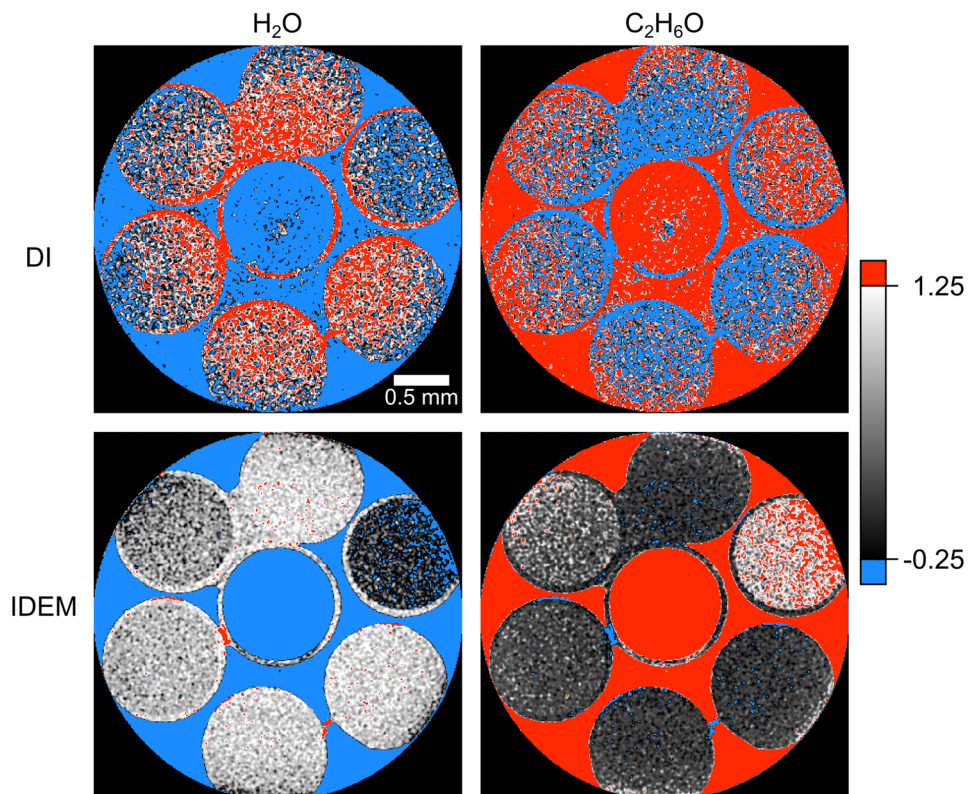


# 6 Conclusion

This study focused on assessing the feasibility of applying DECT material decomposition on dual-target CT data of low-Z samples at high resolution, specifically in the Rigaku nano3DX. Tests on simulated data verified that even for mixtures of two materials with similar attenuation characteristics, material decomposition can be performed with a high-enough sensitivity to estimate their concentrations accurately. The simulated tests were then supported by results obtained with real data. Despite additional variables like dataset alignment, physical effects such as evaporation and beam hardening, and constraints of the scan field of view,

**Table 4** Mean values of concentrations and STDs in decomposed images for real measurements

| RoI | DI $H_2O$ | DI $C_2H_6O$ | IDEM $H_2O$ | IDEM $C_2H_6O$ |
|---|---|---|---|---|
| 1 | $1.007 \pm 0.736$ | $0.009 \pm 0.926$ | $0.879 \pm 0.142$ | $0.167 \pm 0.115$ |
| 2 | $0.003 \pm 0.716$ | $1.057 \pm 0.903$ | $0.048 \pm 0.286$ | $0.937 \pm 0.307$ |
| 3 | $1.033 \pm 0.699$ | $0.045 \pm 0.878$ | $0.879 \pm 0.136$ | $0.161 \pm 0.108$ |
| 4 | $0.963 \pm 0.712$ | $0.023 \pm 0.894$ | $0.833 \pm 0.133$ | $0.195 \pm 0.103$ |
| 5 | $0.599 \pm 0.466$ | $0.466 \pm 0.896$ | $0.756 \pm 0.137$ | $0.251 \pm 0.110$ |
| 6 | $0.428 \pm 0.595$ | $0.595 \pm 0.888$ | $0.566 \pm 0.198$ | $0.411 \pm 0.192$ |

it was possible to apply DTCT material decomposition in a realistic setting. These results encourage further exploration of novel approaches in the field of DECT and applications of material decomposition for quantifying low-Z materials at high resolution using DTCT, as well as further exploration of various artifact and noise reduction techniques in the context of this modality.

## Declarations

**Ethical Approval** not applicable

**Availability of Data and Materials** Data generated for this work can be obtained from the corresponding author upon reasonable request.

## References

1. Heismann, B.J., Schmidt, B.T., Flohr, T.: Spectral computed tomography, SPIE Press, Bellingham. Wash (2012). https://doi.org/10.1117/3.977546

2. Rebuffel, V., Dinten, J.-M.: Dual-energy x-ray imaging: benefits and limits. Insight - Non-Destructive Testing Cond. Monit. **49**(10), 589–594 (2007)

3. Mendonca, P.R.S., Lamb, P., Sahani, D.V.: A flexible method for multi-material decomposition of dual-energy CT images. IEEE Trans. Med. Imaging **33**(1), 99–116 (2014)

4. T. Fuchs, P. Keßling, M. Firsching, F. Nachtrab, G. Scholz, Industrial applications of dual x-ray energy computed tomography (2x-CT), in: Nondestructive Testing of Materials and Structures, Vol. 6, Springer Netherlands, 2011, pp. 97–103, series Title: RILEM Bookseries. https://doi.org/10.1007/978-94-007-0723-8_13

5. D. Vavrik, J. Jakubek, I. Kumpova, M. Pichotka, Dual energy CT inspection of a carbon fibre reinforced plastic composite combined with metal components, Case Studies in Nondestructive Testing and Evaluation 6 (2016) 47–55. https://doi.org/10.1016/j.csndt.2016.05.001 https://linkinghub.elsevier.com/retrieve/pii/S2214657116300107

6. Y. Takeda, K. Hamada, A primer on the use of the nano3dx high-resolution x-ray microscope, Rigaku J (2015)

7. M. Zemek, P. Blažek, J. Šrámek, J. Šalplachta, T. Zikmund, P. Klapetek, Y. Takeda, K. Omote, J. Kaiser, Voxel size calibration for high-resolution ct, in: 10th Conference on Industrial Computed Tomography (iCT) 2020, NDT.net, Wels, Austria, 2020, p. 8. https://doi.org/10.58286/25109 https://www.ndt.net/search/docs.php3?id=25109

8. C. Bellon, A. Deresch, C. Gollwitzer, G.-R. Jaenisch, Radiographic simulator artist: Version 2, in: WCNDT 2012, Vol. 17 of 7, NDT.net, Durban, South Africa, 2012, p. 7. www.ndt.net/search/docs.php3?id=12664

9. Handschuh, S., Beisser, C.J., Ruthensteiner, B., Metscher, B.D.: Microscopic dual-energy CT (microDECT): a flexible tool for multichannel ex vivo 3d imaging of biological specimens. J. Microsc. **267**(1), 3–26 (2017). https://doi.org/10.1111/jmi.12543

10. Paziresh, M., Kingston, A.M., Latham, S.J., Fullagar, W.K., Myers, G.M.: Tomography of atomic number and density of materials using dual-energy imaging and the alvarez and macovski attenuation model. J. Appl. Phys. **119**(21), 214901 (2016). https://doi.org/10.1063/1.4950807

11. Alvarez, R.E., Macovski, A.: Energy-selective reconstructions in x-ray computerised tomography. Phys. Med. Biol. **21**(5), 733–744 (1976). https://doi.org/10.1088/0031-9155/21/5/002

12. Q. Ding, T. Niu, X. Zhang, Y. Long, Image-domain multi-material decomposition for dual-energy CT based on correlation and sparsity of material images, Medical Physics 45 (8) (2018) 3614–3626. arxiv:1710.07028 [physics] https://doi.org/10.1002/mp.13001

13. Biswas, R., Sahadath, H., Mollah, A.S., Huq, M.F.: Calculation of gamma-ray attenuation parameters for locally developed shielding material: Polyboron. J. Radiation Res. Appl. Sci. **9**(1), 26–34 (2016)

14. B. Heismann, L. Bätz, K. Pham-Gia, W. Metzger, D. Niederlöhner, S. Wirth, Signal transport in computed tomography detectors, Nuclear Instruments and Methods in Physics Research Section A:

Accelerators, Spectrometers, Detectors and Associated Equipment 591 (1) (2008) 28–33. https://doi.org/10.1016/j.nima.2008.03.018 https://linkinghub.elsevier.com/retrieve/pii/S016890020800394X

15. J. C. A. Barata, M. S. Hussein, The moore-penrose pseudoinverse. a tutorial review of the theory, Brazilian Journal of Physics 42 (1) (2012) 146–165., https://doi.org/10.1007/s13538-011-0052-z arXiv: 1110.6882 [math-ph]

16. Lee, H., Kim, H.-J., Lee, D., Kim, D., Choi, S., Lee, M.: Improvement with the multi-material decomposition framework in dual-energy computed tomography: A phantom study. J. Korean Phys. Soc. **77**(6), 515–523 (2020). https://doi.org/10.3938/jkps.77.515

17. Jiang, Y., Zhang, X., Sheng, K., Niu, T., Xue, Y., Lyu, Q., Xu, L., Luo, C., Yang, P., Yang, C., Wang, J., Hu, X.: Noise suppression in image-domain multi-material decomposition for dual-energy CT. IEEE Trans. Biomed. Eng. **67**(2), 523–535 (2020)

18. Petrongolo, M., Zhu, L.: Noise suppression for dual-energy CT through entropy minimization. IEEE Transactions on Medical Imaging **34**(11), 2286–2297 (2015)

19. Xue, Y., Ruan, R., Hu, X., Kuang, Y., Wang, J., Long, Y., Niu, T.: Statistical image-domain multimaterial decomposition for dual-energy CT. Med. Phys. **44**(3), 886–901 (2017). https://doi.org/10.1002/mp.12096

20. S. L. Brunton, J. N. Kutz, Data-Driven Science and Engineering: Machine Learning, Dynamical Systems, and Control, 1st Edition, Cambridge University Press, 2019. https://doi.org/10.1017/9781108380690 https://www.cambridge.org/core/product/identifier/9781108380690/type/book

21. Feldkamp, L.A., Davis, L.C., Kress, J.W.: Practical cone-beam algorithm. J. Opt. Soc. Am. A **1**(6), 612 (1984)

22. van Aarle, W., Palenstijn, W.J., De Beenhouwer, J., Altantzis, T., Bals, S., Batenburg, K.J., Sijbers, J.: The astra toolbox: a platform for advanced algorithm development in electron tomography. Ultramicroscopy **157**, 35–47 (2015). https://doi.org/10.1016/j.ultramic.2015.05.002

23. W. Van Aarle, W. J. Palenstijn, J. Cant, E. Janssens, F. Bleichrodt, A. Dabravolski, J. De Beenhouwer, K. Joost Batenburg, J. Sijbers, Fast and flexible x-ray tomography using the ASTRA toolbox, Optics Express 24 (22) (2016) 25129. https://doi.org/10.1364/OE.24.025129 https://opg.optica.org/abstract.cfm?URI=oe-24-22-25129

24. Park, H.S., Chung, Y.E., Seo, J.K.: Computed tomographic beam-hardening artefacts: mathematical characterization and analysis, Philosophical Transactions of the Royal Society A: Mathematical. Phys. Eng. Sci. **373**(2043), 20140388 (2015). https://doi.org/10.1098/rsta.2014.0388